ACS NANO

www.acsnano.org

ARTICLE

Porous but Mechanically Robust All-Inorganic Antireflective Coatings Synthesized using Polymers of Intrinsic Microporosity

Cheng Ji, Zhongbo Zhang, Khalil D. Omotosho, Diana Berman, Byeongdu Lee, Ralu Divan, Supratik Guha,* and Elena V. Shevchenko*

Cite This: *ACS Nano* 2022, 16, 14754−14764

Read Online

ACCESS | Metrics & More | Article Recommendations | Supporting Information

ABSTRACT: **Here, we introduce polymer of intrinsic microporosity 1 (PIM-1) to design single-layer and multilayered all-inorganic antireflective coatings (ARCs) with excellent mechanical properties. Using PIM-1 as a template in sequential infiltration synthesis (SIS), we can fabricate highly uniform, mechanically stable conformal coatings of AlO_x with porosities of ∼50% and a refractive index of 1.41 compared to 1.76 for nonporous AlO_x that is perfectly suited for substrates commonly used in high-end optical systems or touch screens (e.g., sapphire, conductive glass, bendable glass, etc.). We show that such films can be used as a single-layer ARC capable of reduction of the Fresnel reflections of sapphire to as low as 0.1% at 500 nm being deposited only on one side of the substrate. We also demonstrate that deposition of the second layer with higher porosity using block copolymers enables the design of graded-index double-layered coatings. AlO_x structures with just two layers and a total thickness of less than 200 nm are capable of reduction of Fresnel reflections under normal illumination to below 0.5% in a broad spectral range with 0.1% reflection at 700 nm. Additionally, and most importantly, we show that highly porous single-layer and graded-index double-layered ARCs are characterized by high hardness and scratch resistivity. The hardness and the maximum reached load were 7.5 GPa and 13 mN with a scratch depth of about 130 nm, respectively, that is very promising for the structures consisting of two porous AlO_x layers with 50% and 85% porosities, correspondingly. Such mechanical properties of coatings can also allow their application as protective layers for other optical coatings.**

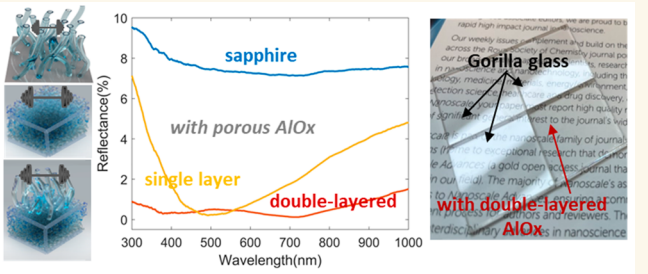

KEYWORDS: *Antireflective coatings, optical coating, low refractive index, porous alumina, polymer of intrinsic microporosity, PIM-1, sequential infiltration synthesis*

INTRODUCTION

Antireflective coatings (ARCs) are widely used to reduce the light reflection at interfaces, and thereby enhance the transmittance of light.[1,2] ARCs with low refractive indices are important for a broad range of applications such as solar cells, displays (mobile phones, computer and television screens), telescope lenses, cameras, and eyeglasses.[3] The optical components in such devices are often made out of different types of glass with varying refractive indices, n, (e.g., fused glass (n = 1.458), sapphire glass (n = 1.768), Gorilla glass (n = 1.50), indium tin oxide (ITO) glass (n = 1.827) at 630 nm).

According to the Fresnel equation,[4] to minimize the reflectance of glass substrates in the visible range of the light spectrum, a single-layer ARC with $n \sim 1.2-1.4$ is required. The optimal thickness of the ARC for a given wavelength λ is $\sim \frac{\lambda}{4n}$ at normal incidence for destructive interference, which leads to minimal reflectance over the spectral range around λ.

Bulk inorganic materials with $n < 1.4$ are limited and mainly restricted to fluorides.[5] For example, MgF_2[6] with $n \sim 1.38$ in the visible range can lower the reflectance of each side of the float glass from 4.3% to 1%. However, MgF_2 thin film deposition involves the use of hydrofluoric acid[7,8] or other aggressive precursors of fluorine.[9] Additionally, MgF_2 is somewhat soluble in water (∼0.013 g/100 mL)[10] and exposure

Received: June 7, 2022
Accepted: August 24, 2022
Published: September 1, 2022

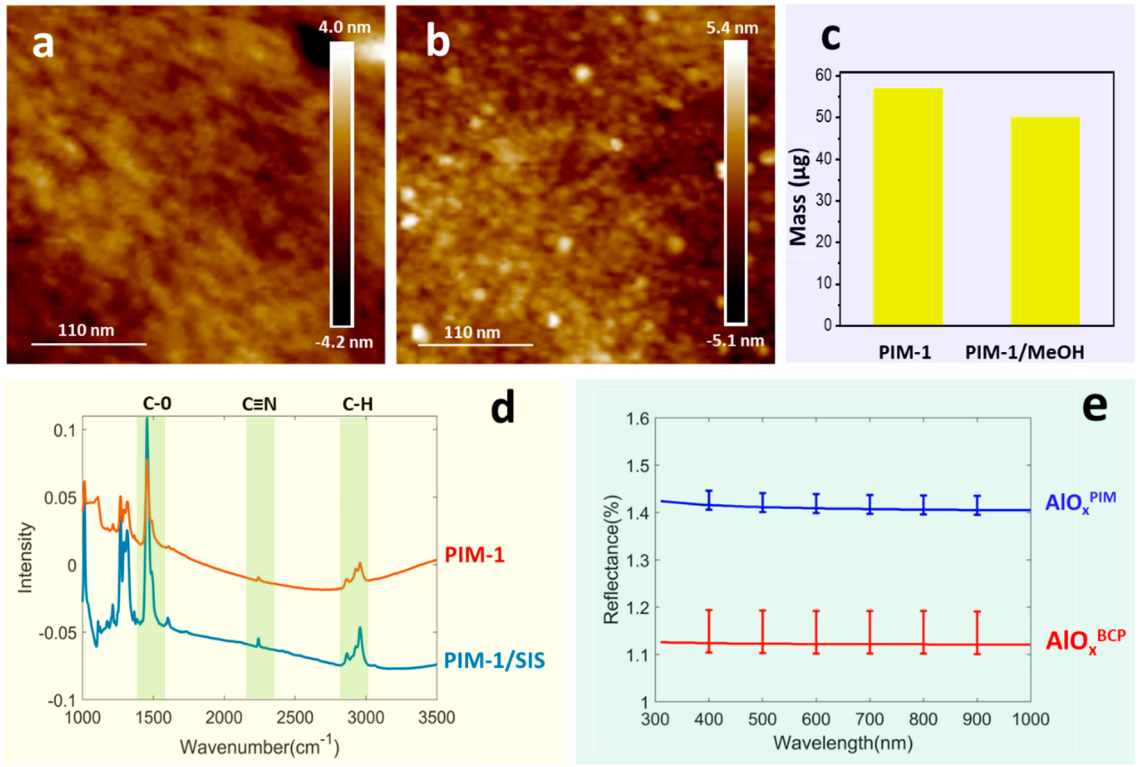

Figure 1. AFM images (a) of as-spin-coated PIM-1 template (b) and PIM-1 templates after methanol treatment for 1 h at 55 °C; QCM data (c) on PIM-1 template before and after methanol treatment; FTIR spectra (d) of as spin-coated PIM-1 and infiltrated PIM-1 with AlO_x; the refractive indices measured using ellipsometry (e) of nanoporous AlO_x film obtained via infiltration of PIM-1 (AlO_x^{PIM}) and PS(79)-PVP(36.5) (AlO_x^{BCP}) followed by polymer removal via annealing.

to inorganic fluorides can be associated with health concerns.[10,11] These factors reasonably impose some constraints on the applicability of fluorides in the fabrication of touchable devices and optical systems exposed to the environment. To achieve safe, nontoxic and stable coatings with lower refractive indexes, nanoporous thin films have been introduced for the fabrication of ARCs.[13−15] According to effective medium theory, the refractive index of the thin composite film is determined by the fractions of different materials as long as the feature sizes are much smaller than the wavelength of the incident light.[16] In the case of dry porous films, their refractive indices will be determined by the refractive index of the inorganic material and air with the refractive index of 1. The higher porosity will be associated with the smaller refractive index. Therefore, proper control over the porosity is the key to nanoporous ARCs with the desired antireflectivity.

Compared to the single-layered ARCs, which can only reduce the reflection in a narrow spectral range, multilayered ARCs consisting of several alternating layers with different thicknesses and refractive indices can provide a better antireflection performance by minimizing the light reflection in a broad spectral range as a result of the destructive interference of wavefronts reflected at each interface. In turn, a gradual decrease of the refractive index (graded-index ARCs) allows for avoiding a sharp transition between interfacing optical media resulting in minimal Fresnel reflection losses.[17] The conventional techniques used to fabricate ARCs include layer-by-layer deposition of low index materials with vacuum coating techniques.[18−20] This technology can produce ARCs with industrial-level optical and mechanical performance. However, the significant drawback is the resulting high cost for the high-quality multilayer structures. Alternative techniques, including nanoporous thin film via polymer with porosities[21] and lithography-produced nanostructure coatings,[22,23] have also been researched for high-quality ARCs. However, porosity can compromise the mechanical properties of materials resulting in increased brittleness, lower hardness and scratch resistance.[24] Moreover, due to the high optical contrast between scratched and unscratched areas originated from differences in the refractive index, the ARCs are subject to high scratch visibility.[25] It is equally important for optical coatings to have adequate mechanical properties in terms of hardness and abrasion resistance in order to withstand day-to-day handling.[26] Therefore, it is critical to develop approaches that can finely tune the refractive index and thickness of the nanoporous inorganic coatings used to design graded-index multilayer ARCs, while preserving the low cost and suitability for large-scale manufacturing of advanced thin films with good resistance to mechanical wear.

Infiltration of block copolymers (BCPs) with inorganic precursors from the vapor phase (sequential infiltration synthesis, SIS) followed by polymer removal was previously shown by us to enable the fabrication of low refractive index nanoporous all-inorganic thin films.[13] However, as it is shown below the mechanical properties of such structures require improvement. Here, we introduce a member of a class of polymers with intrinsic microporosity (PIM), such as PIM-1[27,28] that has pores smaller than 2 nm[29] and high gas permeability[30,31] fostering the infiltration of the polymer template with the precursors from the vapor phase, as a template for the design of mechanically robust highly porous

https://doi.org/10.1021/acsnano.2c05592
ACS Nano 2022, 16, 14754−14764

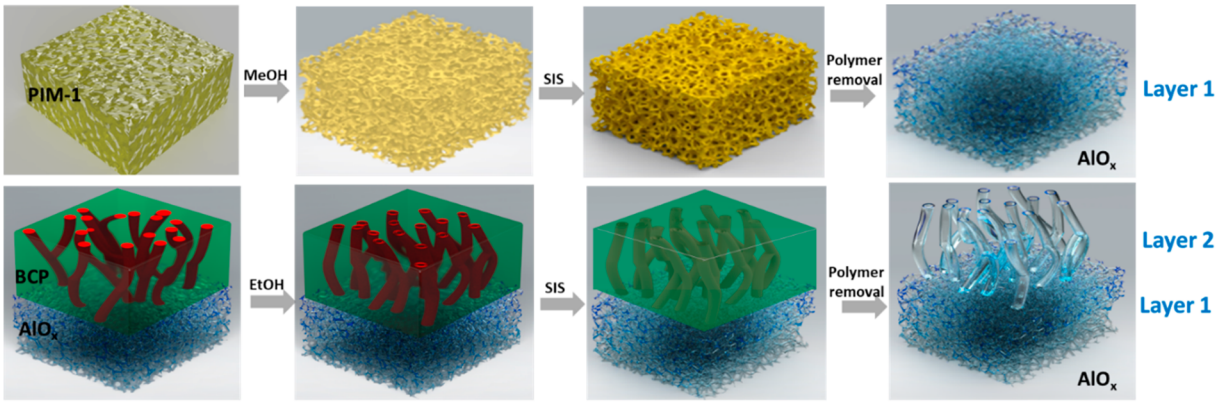

Figure 2. Depiction of the steps involved in the fabrication of single-layer and double-layered AlO_x ARCs using PIM-1. PIM-1 serves as a template for the synthesis of the porous AlO_x (Layer 1). More porous structures can be deposited on the top of Layer 1 using BCP as a template for the formation of more porous double-layered structures.

all-inorganic single coatings with the refractive index of ∼1.41 that is well suited for high refractive index glasses that are crucial for high-end optical systems.[17] We show that such films can be used as a single-layer ARC capable of reduction of the Fresnel reflections of sapphire to as low as 0.1% at 500 nm being deposited only on one side of the substrate. We also demonstrate that PIM templates can be used in combination with the BCP templates, enabling the design of graded-index ARCs. AlO_x structures with just two layers and a total thickness of ∼200 nm are capable of reduction of Fresnel reflections under normal illumination to below 0.5% in a broad spectral range with 0.1% reflection at 700 nm. In addition, we show that optical all-inorganic porous alumina coatings fabricated using PIM-1 templates demonstrate promising mechanical properties revealing a hardness of ∼7.5 GPa. The maximum reached load was 13 mN with a scratch depth of ∼130 nm, a promising value for highly porous films consisting of AlO_x layers with 50% and 85% porosities.

RESULTS AND DISCUSSION

PIM-1 as a Template for Single Layer Alumina ARCs. PIMs have been studied in the past[32,33] because of their potential for CO_2 adsorption.[34] Researchers have infiltrated metal oxide networks into PIMs mostly for mechanical purposes of reinforcing the PIM structure[34−36] or constricting swelling.[32] In our case, we use PIMs as a degradable three-dimensional scaffold or template that allows us to infiltrate metal oxide precursors, burn the PIM off, leaving fully inorganic metal oxide films with the desired porosity.

Our initial results indicated a low efficiency of infiltration of metal oxide precursors into spin-coated PIM-1 layers (it was evidenced by the formation of very thin (∼20 nm) alumina films after polymer removal) unless alcohol treatment of the polymer was performed. Methanol treatment of PIM-1 was reported to increase the free volume in the polymer template[37] and increase gas permeability[38] that can facilitate the infiltration process. Therefore, we immersed the substrates with the ∼60 nm thick spin-coated PIM-1 films into methanol heated up to 55 °C for 1 h that resulted in an increase in the thickness of the polymer film. The thickness of 60 nm for the PIM-1 films was chosen experimentally as one that allows achieving the targeted 80 nm thickness of the final AlO_x coating.

The atomic force microscopy (AFM) analysis performed on the PIM-1 film indicated that the spin-coated films are uniform with sub-nm roughness and some ordering of the structure (Figure 1a). The methanol treatment of the PIMs (see the "Experimental Details" section), however, affects the morphology of the conformal PIM-1 coating, resulting in an increased roughness and a loss of the structural ordering in the polymer template (Figure 1b, Figure S1). It appears that methanol treatment leads to the densification of some structural elements of PIM-1 into sphere-like aggregates, thereby increasing the free space dispersed within the volume of the polymer. These transformations are on the order of sub-nm length scales, and therefore not expected to affect the optical properties of the material in the visible part of the optical spectrum. We also used quartz crystal microbalance (QCM) analysis to monitor the change in mass of PIM-1 as a result of the methanol treatment (Figure 1c). The QCM data showed a small decrease in the mass of the PIM-1 after the methanol treatment (Figure 1c). We attribute this to the removal of small amounts of oligomers possibly present in original PIM-1 or solvent molecules (chloroform) possibly trapped in the polymer matrix. As it was mentioned, we, indeed, observed that methanol treatment of PIM-1 improved its infiltration efficiency with trimethylaluminum (TMA) as evidenced by the thicker AlO_x films formed after polymer removal. Therefore, we performed methanol treatment for all PIM-1 samples. The X-ray photoelectron spectroscopy (XPS) results (Figure S2) indicate that a small number of methanol molecules can be trapped in the structure of PIM-1 as a result of its methanol treatment that can, in turn, also facilitate the deposition of AlO_x via providing polar groups for interaction with TMA.[39]

The Fourier transform infrared (FTIR) data (Figure 1d) shows that the peak positions do not shift after 10 SIS cycles, which implies that the alumina precursors from the infiltration synthesis intertwined with the PIM polymer chains without forming chemical bonds.[32] Exposure of PIM-1 to TMA likely results in the interactions of C≡N bonds with TMA molecules[32,36] that is also confirmed by theoretical calculations.[36] It was proposed that metal oxide clusters could percolate throughout the hybrid structure without the formation of chemical bonds with the PIM-1 polymer via nucleation of semipermanent metal−organic adducts of metal oxide precursors with PIM-1's C≡N groups.[32] Upon water

https://doi.org/10.1021/acsnano.2c05592
ACS Nano 2022, 16, 14754−14764

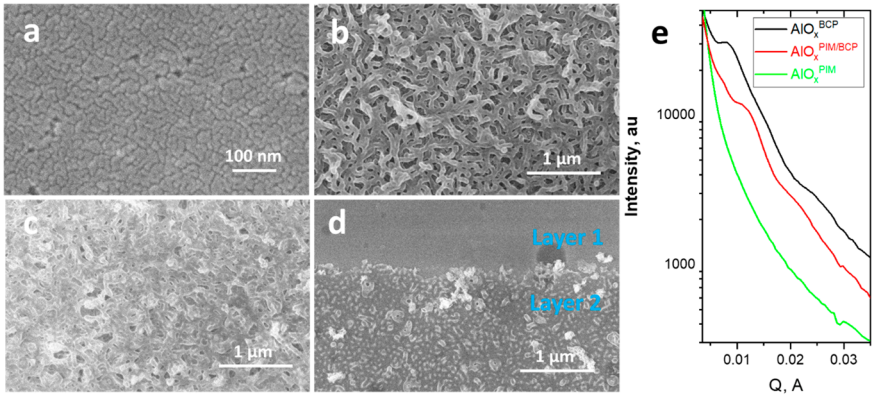

Figure 3. SEM images of single 80 and 105 nm thin AlO$_x$ layers formed as a result of 10 SIS cycles on PIM-1 (AlO$_x^{PIM}$, Layer 1) and (AlO$_x^{BCP}$, Layer 2) (panels a and b, respectively). (c) SEM image of the double-layered AlO$_x$ ARC (AlO$_x^{PIM/BCP}$). (d) Top view SEM image showing the interface between AlO$_x$ layers with different porosities in double-layered AlO$_x$ ARC (bottom and top layers were ∼80 and 105 nm, respectively). (e) SAXS data obtained for AlO$_x$ layers shown in panels a−c.

exposure in the second half of the SIS cycle, the aluminum oxide clusters are formed and become unbonded from the C≡N bonds[32] still forming a porous scaffold of AlOx. This mechanism is different from the mechanism reported for SIS when BCP polymer templates are used.[39−41] After deposition of BCP polymer, polar and nonpolar parts of BCP molecules phase-segregate forming patterns determined by the characteristics of the BCP molecules.[42,43] Note that in the case of BCPs templates, the peak positions corresponding to, for example, C=O and −C−O−R groups in polar domains of BCPs were found to shift upon BCPs exposure to the vapors of TMA or other metal precursors indicating the formation of chemical bonds with TMA.[41,44] For example, in the case of PS(79)-PVP(36.5) during the infiltration cycles, the TMA precursors interact mainly with functional groups of polar domains formed by P4VP, while no infiltration into PS domains occurs, leading to selective infiltration of polar domains of PS(79)-PVP(36.5) used in our study. Since the size of polar and nonpolar parts of selected for our application BCP molecules is in the nanometer range, further polymer removal leads to the formation of nanoporous AlO$_x$ structures, as shown in our previous study.[13] Here 10 cycles of SIS was found to be sufficient to achieve the desired optical and mechanical properties in the final alumina conformal coating.

After an annealing treatment at 500 °C under airflow for 3 h, the PIM-1 template was removed and only a porous AlO$_x$ scaffold (AlO$_x^{PIM}$) was left on the substrate (Figure 2, Figure S3). The final porosity of alumina film formed via 10 SIS cycles was ∼50%. The thickness of the alumina film was estimated by ellipsometry to be ∼80 nm. The scanning electron microscopy (SEM) data indicates that the obtained alumina films (deposited on silicon) are smooth (Figure 3a). Small-angle X-ray scattering (SAXS) data show that AlO$_x$ obtained using the PIM-1 template has a mesoscale poorly ordered structure (Figure 3e). A very broad peak at the higher Q region suggests the presence of spherical features of ∼10 nm with a rather broad size distribution in the AlO$_x$ layer that agrees with the SEM data (Figure 3a). The PIM-1 layer during spin coating can trap air between the polymer and the substrate. During the polymer removal via thermal annealing, such areas slightly deflate forming darker circular features in the SEM images obtained on AlO$_x^{PIM}$ (Figure 3d, Figure S4). Energy dispersive spectroscopy (EDS) mapping data show the uniform distribution of Al and O (Figure S4). Analysis of delaminated fragments of the AlO$_x^{PIM}$ films by SEM also points to a uniform nature of the porous coating. Importantly, such features do not affect the deposition of the consecutive layers (Figures 3d, S4, and S5). The refractive index of 80 nm porous alumina single layer with 50% porosity obtained with the PIM-1 template is ∼1.41 in the spectral range between 300 and 1000 nm (Figure 1e). Such a refractive index is well suited to minimize the reflectance for high refractive index substrates such as sapphire (n = 1.768) or ITO glass (n = 1.827).

Graded-Index Double-Layered Alumina ARCs. To further decrease the reflectance of the sapphire glass, we deposited the second porous layer using BCP as a template,[13] which enables the fabrication of porous coatings with a porosity above 50%.[13] For that, we spin-coated a 50 nm thick PS(79)-PVP(36.5) film on the porous AlO$_x$ layer obtained using the PIM-1 template (Figure 2). The nonsolvent swelling treatment of BCP was conducted to increase the infiltration depth of the polymer and the porosity of the final metal oxide thin film.[45,46] The infiltration mechanism of BCPs has been previously described in detail.[13,47−49] Here 10 SIS cycles were applied to infiltrate the PS-P4PV with alumina precursors; after that, the polymer template was removed via 1 h thermal annealing, resulting in the formation of the double-layered gradient structure. The film thickness of porous alumina was estimated by ellipsometry to be ∼105 nm. SEM data indicated that alumina coatings obtained using PS-P4VP templates consisted of rather tangled porous tubular micelles (Figure 3). The porosity of the second layer was estimated by ellipsometry measurements to be 85%. To visualize the interface between AlO$_x^{PIM}$ and AlO$_x^{BCP}$ in AlOx$^{PIM/BCP}$, we prepared the sample shown in Figure 3d in which we mechanically removed the fragment of PS(79)-PVP(36.5) film spin-coated on the top of AlO$_x^{PIM}$ before SIS.

SAXS data indicates that being deposited on porous AlO$_x^{PIM}$ (Layer 1), AlO$_x^{BCP}$ (Layer 2) has a smaller domain spacing as compared to that deposed directly on the Si substrate. The SAXS pattern from of AlO$_x^{BCP}$ grown directly on Si and the position of the diffraction peak from its microphase separated cylindrical structure, q = 0.0089 A^{-1} corresponding to d-spacing of 70.5 nm (Figure 2e), are similar to those of neat PS-PVP.[50,51] On the other hand, the SAXS peak from the AlOx$^{PIM/BCP}$ appears at a much higher q, suggesting that the degree of microphase separation of the BCP is suppressed on PIM. However, the SAXS pattern of the AlOx$^{PIM/BCP}$ also

https://doi.org/10.1021/acsnano.2c05592
ACS Nano 2022, 16, 14754−14764

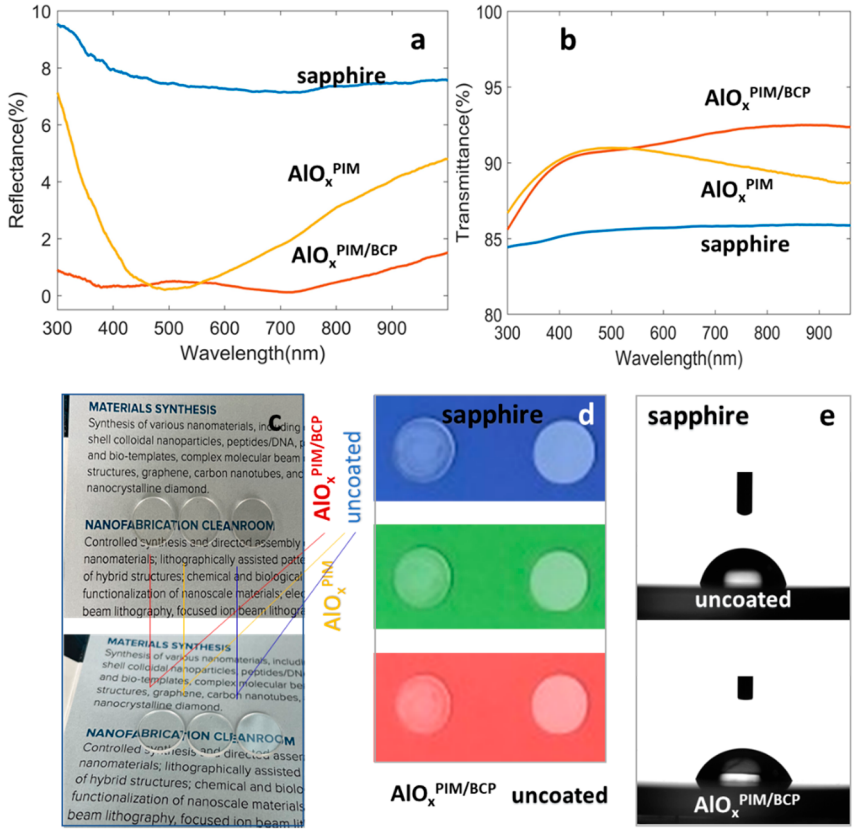

Figure 4. Optical performance of single (AlO_x^{PIM}) and graded-index double-layered ($AlO_x^{PIM/BCP}$) ARCs deposited on sapphire glass: the reflectance (a) and the transmittance (b) data; the optical micrographs (c,d) visualizing the performance of the porous ARCs. The images were taken at normal incidence and at an ∼45° angle (top and bottom, respectively). Images shown in panel d were taken at an ∼45° angle to the substrate. (e) Contact angle measurements on sapphire and sapphire coated with graded-index double-layered ($AlO_x^{PIM/BCP}$) after hexamethyldisilazane (HMDS) treatment.

shows a diminished peak at the same position as AlO_x^{BCP} at q = 0.0089 A^{-1}. Therefore, we conclude that the structures of both samples are not much different from each other at their top surfaces as seen from SEM images (Figure 3b,c), where the morphologies are affected more by the polymer/air interaction than the polymer/substrate interaction.

Optical Properties of the Single- and Graded-Index Double-Layered ARC Coatings. The refractive index of 1.41 characteristic to a porous alumina single layer with 50% porosity obtained with PIM-1 template (Figure 1e) is well suited to minimize the reflectance of high refractive index substrates such as sapphire (n = 1.768) or ITO glass (n = 1.827). Indeed, Figure 4 demonstrates that the reflectance of sapphire can be lowered from ∼7.9% to 0.1% at 500 nm due to the porous alumina coating on only one side of sapphire while the transmittance increased from ∼85% to ∼90−91% in the spectral range between 380 and 650 nm (Figure 4a).

In double-layered ARC coating the thicknesses of Layer 1 and Layer 2 were 80 and 105 nm, respectively. According to the quarter wavelength optimized thickness theory for ARC, these layers should enable destructive interference for the wavelengths in the visible range. Two layers of porous alumina prepared as described (Figure 2) resulted in the design of the graded-index ARC for a sapphire substrate that lowered its reflectance from 7.9% to below 0.5% in a broad spectral range (Figure 4a). Moreover, the reflectance of sapphire was lowered to 0.1% at ∼700 nm. The light transmission of sapphire was increased from ∼85% to ∼91−93% just as a result of deposited ARC on one side of the sapphire. Note that such a significant reduction of the reflectance and increase in the transparency of the sapphire was realized by deposition of only two gradient-index layers with a total thickness smaller than 200 nm. Photographs of the uncoated and coated sapphire glass are shown in Figure 4c,d to visualize the performance of the single-layer and graded-index double-layered ($AlO_x^{PIM/BCP}$) and to highlight the better transparency and less reflection of the sapphire coated with porous ARCs.

The double-layered ARC worked well also for the Gorilla glass (n = 1.50), which is one of the commercial glass candidates for high-performance screens.[52] With only just two layers of porous AlO_x, we observed in our double-layered structure ($AlO_x^{PIM/BCP}$) a significant reduction of the reflectance at normal incidence from 4% to below 0.8% over the visible range (Figure 5a). The transmittance was improved from 92% to above 95% in the visible range with just a single side coating (Figure 5b). Figure 5c shows the optical image of Gorilla glass coated with graded-index double-layered ARC, demonstrating the transparency of the coated sample and elimination of the light reflection at the substrate coated with double-layered $AlO_x^{PIM/BCP}$ ARC. One can see no reflection of the light at the coated substrate, while surrounding uncoated Gorilla glass samples demonstrate the pronounced reflection (Figure 5c, bottom image).

https://doi.org/10.1021/acsnano.2c05592
ACS Nano 2022, 16, 14754−14764

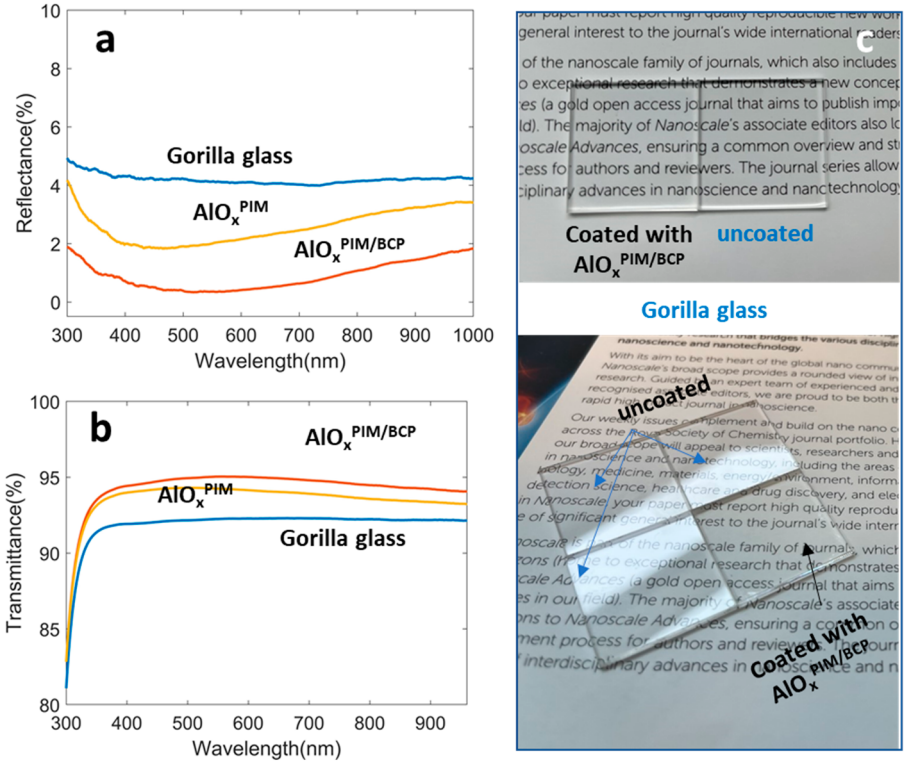

Figure 5. Optical performance of single (AlO_x^{PIM}) and graded-index double-layered ($AlO_x^{PIM/BCP}$) ARCs deposited on Gorilla glass: the reflectance (a) and the transmittance (b) data; optical images of Gorilla glass sample with graded-index double-layered ($AlO_x^{PIM/BCP}$) ARCs obtained at normal incidence (top image) and at ~30° angle (bottom image). Figure 6c (bottom image) shows the elimination of the reflection at the coated substrate while the reflection of the fluorescent light tube is pronounced at the surrounding uncoated substrates.

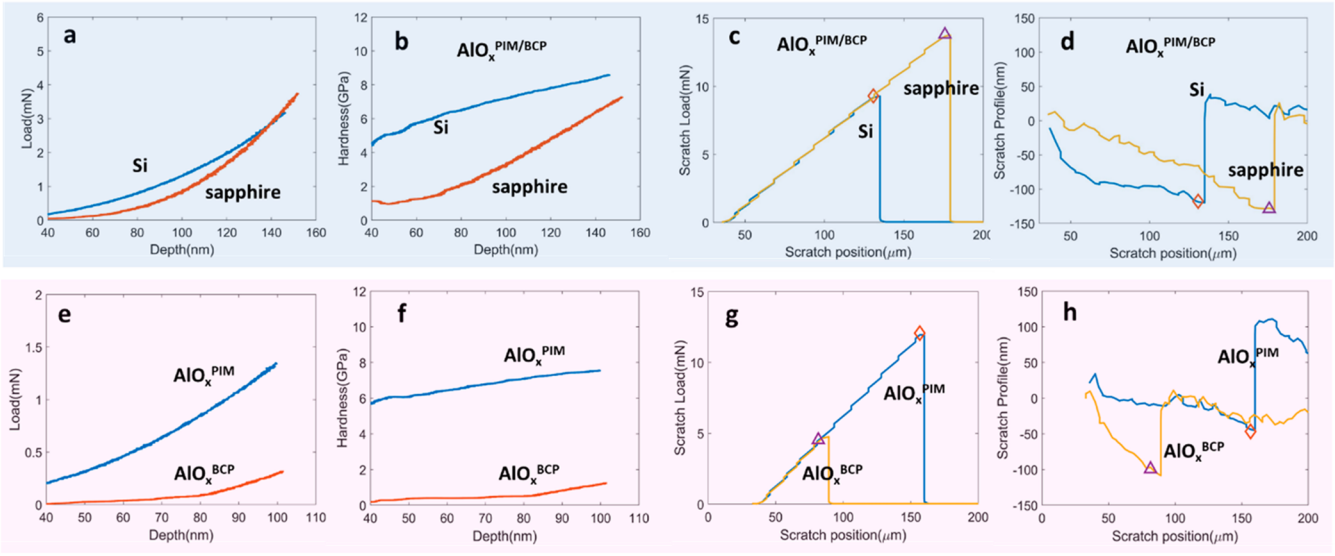

Figure 6. Mechanical properties of the graded-index double-layered 185 nm ARCs structures ($AlO_x^{PIM/BCP}$) deposited on different substrates (Si and sapphire) (a–d): (a) the exerted load vs nanoindentation depth and (b) the thin film hardness vs nanoindentation depth. (c) The scratch load vs the scratch position during the nano scratch test. The critical markers show the point when the pinhead is lifted off the surface. (d) The vertical scratch profile vs the scratch position during the nano scratch test shown in panel c. The comparison of the mechanical properties of AlO_x^{PIM} (Layer 1 in double-layered ARC) and AlO_x^{BCP} (Layer 2 in double-layered ARC) on Si (e–h): (e) The exerted load vs nanoindentation depth. (f) The thin film hardness vs nanoindentation depth. (g) The scratch load vs the scratch position during the nano scratch test. The critical markers show the point when the pinhead is lifted off the surface. (h) The vertical scratch profile vs the scratch position during the nano scratch test, shown in panel g. The comparison shows that the AlO_x^{PIM} layer has much higher hardness and scratch resistance as compared to AlO_x^{BCP}.

Therefore, the experimental results reveal that our double-layered structure synthesized through the infiltration of two

https://doi.org/10.1021/acsnano.2c05592
ACS Nano 2022, 16, 14754–14764

types of polymer templates sufficiently reduced the reflection of the typical optical substrates such as sapphire (n = 1.768) and Gorilla glass (n = 1.50) over a broad wavelength range.

Mechanical Properties of the Single- and Graded-Index Double-Layered Porous Alumina Coatings. Mechanical properties of the ARC coatings need to be appropriate for protection against scratches and abrasion during their use. We measured the hardness and scratch resistance of our films, parameters commonly used to characterize the mechanical performance of the optical coatings.[20,53] While we were mostly interested in the mechanical properties of graded-index double-layered porous films on sapphire, we also studied such structures deposited on Si.

Our hardness and scratch test results (Figure 6) indicate that despite the porous nature our PIM-templated and PIM/BCP double-layered coatings have excellent mechanical properties and are superior to the BCP-only coatings. Figure 6a shows the plots of the hardness versus the nanoindentation depth. The hardness of graded-index double-layered ARC structures ($AlO_x^{PIM/BCP}$) on sapphire at a nanoindentation of 150 nm can be as high as 7.5 GPa (Figure 6b), which is, in fact, higher than the hardness of, for example, bulk fused silica glass (~6 GPa).[54] Note, the hardness of sapphire (α-alumina) is around 20 GPa.[12] Conducting the hardness measurements on AlO_x deposited on different substrates, we observed the effect of the substrate on the hardness that is expected for thin films.[55] Interestingly, at smaller loads AlO_x deposited on sapphire shows a higher tendency toward its deformation, as evidenced by lower hardness than coatings deposited on the Si (Figure 6b). Since sapphire has a higher hardness than Si, the effect of the substrate only should result in the opposite trend. However, at higher loadings the hardness values of both coatings start to be similar for graded-index double-layered porous coatings deposited on sapphire and Si substrates and therefore we propose that this observation can be associated with the position of sharp Berkovich-type indenter with respect to the pores in the top layer and orientation of the pores. In general, in order to minimize the effect of the substrate, it is recommended to analyze samples in which the deformation takes place only in the top 10−20% of the volume.[55,56] This is, however, an unreasonable condition for our structures that have a thickness below 200 nm, dictated by the optical needs of the application.

Figure 6c shows the scratch load during the scratching tests. In such tests the critical load can be used as a measure to compare the scratch resistivity of different coatings if the experimental parameters are kept constant. The maximum load is detected by the instrument using acoustic emission feedback picked by a piezoelectric detector arranged next to the indenter. The maximum reached load was 13 mN with a scratch depth of about 130 nm (Figure 6d), which is much higher than that of the porous anodic aluminum oxide (AAO) ARC structures in which the indenter can penetrate down to 350 nm at 2 mN load,[57] and approximately two times better than we achieved for optical coatings on commercial lenses tested using the same testing parameters. (Figure S6, Supporting Information). The scratch tests indicated higher scratch resistivity of coatings deposited on the sapphire substrate as compared to coatings on Si (Figure 6c,d) that is reasonable since sapphire and the graded-index double-layered coating have a similar chemical composition that can result in their better adhesion of the coatings to the substrate.

Our results indicate that the films containing PIM (whether single layer or double-layered) are significantly harder (Figures 6a,e). The advanced mechanical properties of graded-index ARC are most likely due to the underlying AlO_x^{PIM} (Layer 1) formed via infiltration of PIM-1 (Figure 6f). The hardness of AlO_x^{PIM} is much higher than that of AlO_x^{BCP} and comparable to the hardness of the double-layered ARCs on Si (Figure 6b). The scratch test data demonstrate the same trend (Figure 6c). Therefore, Layer 1 fabricated via SIS in PIM not only served as the first antireflection layer with a higher refractive index as expected but also performed as a mechanical supporting layer for the porous film above it. The higher hardness and scratch resistance of the AlO_x^{PIM} films as compared to AlO_x^{BCP} films can be attributed to their lower porosity and smaller size of the pores. The mechanical test results on the double layer ARCs on Gorilla glass are presented in the Supporting Information (Figure S7).

The videos visualizing the mechanical stability of the gradient-index double-layered ARC under standard cleaning procedures are given in the Supporting Information (Video 1 and Video 2). Note, the double-layered coatings shown in both videos were deposited on a Si substrate. Porous AlO_x coatings being deposited on Si are colored due to light interference between the light reflected from the top and the bottom surfaces of the film deposited on the nontransparent substrate. As a result, it is easier to notice any scratches or delamination in the films on a Si substrate than on transparent sapphire or glass. Videos (Video 1 and Video 2) demonstrate that double-layered coatings can withstand standard cleaning procedures.

It is worth noting that as-prepared double-layered ARCs are hydrophilic; however, they can be hydrophobized by hexamethyldisilazane (HMDS) treatment. Figure 4e shows that such treatment almost "restores" the contact angle of hydrophobic sapphire. Thus, the contact angle of water droplet at sapphire and sapphire with HMDS treated double-layered ARC are ~85° and ~75°, respectively. There also other standard treatments enabling surface hydrophilization that can be applied to an alumina surface if hydrophobicity of the surface is desired.[15]

It is also worth noting that we also conducted sample preparation of graded-index double-layered coatings using annealing of both polymers at once to minimize the number of the steps in this synthetic procedure. The rationale behind this effort was that PIM-1 was expected to have only very slight solubility in the solvent that is used for dissolution of a BCP such as toluene.[38] Moreover, infiltration of PIM-1 with inorganic metal oxides has been previously reported to prevent their solubility even in good solvents (e.g., THF).[22] However, while we were able to construct coating with rather promising optical performance (Figure S8), such samples were different from samples prepared according to the scheme shown in Figure 2. We assume that this is a result of the slight solubility of PIM-1 in toluene even after its infiltration with AlO_x precursors, and further studies on the improvement and simplification of the fabrication process are needed.

CONCLUSION

In conclusion, PIM-1 can be used as a highly promising template for the robust deposition of uniform porous AlO_x conformal films with porosity of ~50% and a refractive index of 1.41 using SIS. Such a refractive index works well for high refractive index substrates (e.g., sapphire, etc.) actively used in optical elements. For instance, a single layer AlO_x coating

https://doi.org/10.1021/acsnano.2c05592
ACS Nano 2022, 16, 14754−14764

obtained using a PIM-1 template deposited only on one side of the substrate reduces the Fresnel reflections of sapphire to as low as 0.1% at 500 nm. Moreover, such layers can be further used in more complex architectures. We also demonstrate that deposition of the second layer with higher porosity using block copolymers enables the design of graded-index double-layered coatings reducing Fresnel reflections under normal illumination to below 0.5% in a broad spectral range with 0.1% reflection at 700 nm. It is achieved by nontoxic, stable AlO_x structures with just two layers and a total thickness of below 200 nm. Single-layer and graded-index double-layered AlO_x ARCs are characterized by high hardness and scratch resistivity. Importantly, the mechanical properties of graded-index double-layered coatings are determined by advanced properties of a mechanically more robust layer formed by infiltration of PIM-1 with a metal oxide precursor. The maximum reached load was 13 mN with a scratch depth of about 130 nm, and that is promising for the structures consisting of two porous AlO_x layers with 50% and 85% porosities, respectively.

The BCP templates enable the control over porosity in a broad range, while porosity of a metal oxide achieved with PIMs is likely to be around 50%. However, the use of PIMs for the fabrication of ARCs offers its own advantages. First, high-end optical systems and products utilize higher refractive index substrates and a refractive index of ∼1.41 is well suited for such substrates. For instance, infiltration of PIM-1 with metal oxide precursors can be used to deposit porous films on sapphire and other structures, such as the ITO glass[58] or flexible borosilicate glass.[59] Second, PIMs can be more cost efficient polymer templates as compared to BCPs: the synthesis of high-quality BCPs assumes the rigorous control over the polymerization reaction and requires purification from traces of homopolymers while the synthesis of PIM-1 is a rather straightforward and simple process.[27] Third, as we show here, porous metal oxide coatings fabricated using the PIM-1 template can have rather advanced mechanical properties. Fourth, the stability of PIMs at a high temperature[60] provides the possibility for the synthesis of various oxides materials, precursors of those are decomposed at higher temperatures, which can further broaden the library of porous materials with lower refractive indices or make porous structures for other applications. The use of PIM-1 as a template results in potentially cost and process-efficient fabrication of coatings combining promising optical and, importantly, mechanical properties.

EXPERIMENTAL DETAILS

Materials. Substrates in the experiments were silicon, sapphire, and Gorilla glass. The silicon substrates with 300 nm thermal oxide were purchased from Silicon Valley Microelectronics, Inc. The half-inch sapphire glass windows were purchased from Meller Optics. Gorilla glass was purchased from Abrisa Technologies. The polymer of intrinsic microporosity such as PIM-1 was synthesized in DMAc at 160 °C following the previously reported procedure.[27] Dimethylacetamide (DMAc, Sigma-Aldrich) and anhydrous potassium carbonate (K_2CO_3, Sigma-Aldrich) were used as received. 5,5′,6,6′-Tetrahydroxy-3,3,3′,3′-tetramethylspirobisindane (TTSBI, Sigma-Aldrich) was purified by crystallization from methanol. Tetrafluoroterephthalonitrile (TFTPN, Sigma-Aldrich) was purified by vacuum sublimation at 150 °C under an inert atmosphere. The block copolymer poly(styrene-*block*-4-vinylpyridine) (PS-P4VP) (specifically in this study (PS(79)-PVP(36.5)) was purchased from Polymer Source, Inc.

Polymer Film Deposition. The dry PIM-1 powder was dissolved in anhydrous chloroform with a concentration of 20 mg/mL. The dry PS(79)-PVP(36.5) powder was dissolved in toluene to obtain 13 mg/mL. After dissolution, the polymer solutions were filtered through a polytetrafluoroethylene (PTFE) 0.45 μm pore size filter and spin-coated onto the clean substrate at 2000 and 4000 rpm for PIM-1 and PS(79)-PVP(36.5), respectively. The cleaning process of the substrates was the following: sonication in DI water (2 min), followed by sonication in acetone (2 min) and in isopropyl alcohol (2 min).

Solution Treatment of the Deposited Polymer. For PIM thin films, the substrates with the deposited coatings were immersed in methanol heated to 55 °C for ∼1 h and then kept at room temperature overnight in a fume hood. For BCP thin films, the samples were immersed in ethanol heated to 75 °C for 2 h. After completion, the samples were dried under nitrogen gas flow and used for infiltration with inorganic precursors from the vapor phase immediately.

Infiltration of the Polymer Templates with Alumina Precursors. The infiltration of polymer templates with alumina precursors was performed using a SIS method that has been described earlier.[13,61−63] A GEMStar thermal atomic layer deposition (ALD) system was used for the process for convenience, though we note that our process is not an ALD process (deposition rates are much higher and the deposition is not atomic layer-by-layer) and could be carried out in other appropriately configured chemical vapor deposition systems as well. TMA and H_2O were used as gas-phase precursors. In the first half of a SIS cycle (∼400s), the TMA vapors (0.08 s pulse length through the ALD actuator) infiltrate into the polymer template, selectively binding to the functional groups.[13] The selectively bound precursors then react with water vapor (0.08 s pulse length through the ALD actuator) locally producing AlO_x in the next half of the synthesis cycle (∼120 s). At the end of each SIS cycle, the unreacted gases are purged out of the chamber with 200 sccm N_2 gas flow for 20 s. The procedure was repeated 10 times. The infiltration was performed at 90 °C. The recipe used in SIS is provided in the Supporting Information (Table S1).

Thermal Annealing. After SIS, the samples were annealed at 500 °C for 1 to 3 h to remove the polymer template under airflow in the quartz tube in a Thermolyne 21100 Tube Furnace.

Fabrication of Single-Layer Alumina ARCs. Single-layer alumina ARCs (further referred as AlO_x^{PIM}) were prepared following the procedures described above.

Fabrication of Graded-Index Double-Layered Alumina ARCs. Graded-index double-layered alumina ARCs, further referred as $AlO_x^{PIM/BCP}$, were prepared via spin-coating of a solution of PS(79)-PVP(36.5) on the top of the porous AlO_x^{PIM} film. The details of the fabrication steps are provided above. For double-layered ARCs, 10 cycles of SIS were exerted both on the PIM and the BCP templates to obtain Layer 1 and Layer 2, respectively. Hexamethyldisilazane (HMDS) treatment was performed using YES-3/5TA. The process parameters were 150 °C, pressure 1 Torr, and 3 cycles of N_2 and HMDS purging for 5 min

Hexamethyldisilazane (HMDS) Treatment. HMDS treatment was performed using YES-3/5TA. The process parameters were 150 °C, pressure 1 Torr, and 3 cycles of N_2 and HMDS purging for 5 min

Characterization. A Horiba Jobin Yvon UVISEL spectroscopic ellipsometer was used to measure the film thickness, porosity, and refractive index of the nanoporous thin film. Refractive indices were measured for at least 5 samples for each type of sample. QCM experiments were conducted for the quantitative analysis of the effect of methanol treatment on the PIM-1 using an SRS QCM200 controller. PS(79)-PVP(36.5) and PIM-1 films were deposited on the titanium QCM substrates via spin-coating of the corresponding polymer solutions. The AFM analysis of the coating morphology was performed with a Bruker Multimode AFM in the tapping mode using a silicon tip (0.5 Hz scanning speed). The SEM images were obtained using a JEOL JSM-7500F microscope. Film reflectance was measured by a Filmetrics F40 thin film analyzer. The transmittance of the samples was characterized using an UV−vis spectrophotometer Cary-

https://doi.org/10.1021/acsnano.2c05592
ACS Nano 2022, 16, 14754−14764

50. The FTIR analysis was performed using a Nicolet 6700 spectrometer. Contact angle measurements were conducted using a Kruss DSA100 drop shape analyzer. The mechanical properties of the thin films were characterized by a KLA iNano nanoindenter. The fused silica reference material was tested for instrument verification. The hardness tests were performed with the Berkovich tip. The scratch tests were performed with a conical tip with a radius of 5 μm by continuously increasing the load on the film as the indenter moved along the surface of the substrate with a velocity of 20 μm/s. The ramp-load started at 0.04 mN and ended upon reaching a load necessary to cause some identifiable film failure (critical load) or until reaching 20 mN if the film did not deform. All scratch tests were run using the same parameters to compare the critical load values from different samples more accurately. The critical load was automatically determined by the instrument using acoustic emission feedback picked by a piezoelectric detector arranged next to the indenter. A critical load was defined as the load value at which the acoustic emission suddenly increased. Depth profiles of the scratch vectors were also recorded and analyzed. SAXS data were collected at beamline 12-ID-B at Advanced Photon Source. The XPS analysis was performed using a PHI 5000 Versaprobe spectrometer with monochromatic 1486.6 eV Al Kα radiation.

ASSOCIATED CONTENT

Supporting Information

The Supporting Information is available free of charge at https://pubs.acs.org/doi/10.1021/acsnano.2c05592.

AFM and XPS data on PIM-1 templates and PIM-1 templates before and after methanol treatment, EDS data on the double-layer ARCs, SEM images of single layer and double-layered AlOx films, the representative mechanical test results on a commercial optical lens with ARC and on Gorilla glass with double-layer ARCs structures, the optical performance of the samples prepared by deposition of the BCP films on the top of PIM-1 and annealed at once; SIS recipe used for infiltration of polymer templates with AlO_x using GEMstar Thermal ALD system (PDF)

Mechanical stability of the gradient-index double-layered ARC under standard cleaning procedure (MP4)

Mechanical stability of the gradient-index double-layered ARC under standard cleaning procedure (MP4)

AUTHOR INFORMATION

Corresponding Authors

Supratik Guha − *Pritzker School of Molecular Engineering, University of Chicago, Chicago, Illinois 60637, United States; Materials Science Division, Argonne National Laboratory, Argonne, Illinois 60439, United States;* orcid.org/0000-0001-5071-8318; Email: guha@uchicago.edu

Elena V. Shevchenko − *Center for Nanoscale Materials, Argonne National Laboratory, Argonne, Illinois 60439, United States; Department of Chemistry and James Franck Institute, University of Chicago, Chicago, Illinois 60637, United States;* orcid.org/0000-0002-5565-2060; Email: eshevchenko@anl.gov

Authors

Cheng Ji − *Pritzker School of Molecular Engineering, University of Chicago, Chicago, Illinois 60637, United States; Materials Science Division, Argonne National Laboratory, Argonne, Illinois 60439, United States*

Zhongbo Zhang − *Pritzker School of Molecular Engineering, University of Chicago, Chicago, Illinois 60637, United States; The Chemical Sciences and Engineering Division, Argonne National Laboratory, Argonne, Illinois 60439, United States;* orcid.org/0000-0001-5294-444X

Khalil D. Omotosho − *Materials Science and Engineering Department and Advanced Materials and Manufacturing Processes Institute, University of North Texas, Denton, Texas 76203, United States*

Diana Berman − *Materials Science and Engineering Department and Advanced Materials and Manufacturing Processes Institute, University of North Texas, Denton, Texas 76203, United States;* orcid.org/0000-0002-9320-9772

Byeongdu Lee − *Advanced Photon Source, Argonne National Laboratory, Argonne, Illinois 60439, United States;* orcid.org/0000-0003-2514-8805

Ralu Divan − *Center for Nanoscale Materials, Argonne National Laboratory, Argonne, Illinois 60439, United States*

Complete contact information is available at: https://pubs.acs.org/10.1021/acsnano.2c05592

Notes

The authors declare no competing financial interest.

ACKNOWLEDGMENTS

The authors thank Liliana Stan (Center for Nanoscale Materials, Argonne National Laboratory) for fruitful discussions and help with atomic layer deposition system, and Michael Talapin (a senior student at Lyons Township High School, District 204) for his help with graphical work. Work performed at the Center for Nanoscale Materials, a U.S. Department of Energy Office of Science User Facility, was supported by the U.S. DOE, Office of Science, Office of Basic Energy Sciences, and Division of Chemical Sciences, Geosciences, and Biosciences under Contract No. DE-AC0206CH-11357. D.B. and K.O. acknowledge the support by the National Science Foundation, Award No. 2045662. S.G. was supported by the Vannevar Bush Fellowship under the program sponsored by the Office of the Undersecretary of Defense for Research and Engineering and in part by the Office of Naval Research as the executive manager for the grant.

REFERENCES

(1) van de Groep, J.; Spinelli, P.; Polman, A. Single-Step Soft-Imprinted Large-Area Nanopatterned Antireflection Coating. *Nano Lett.* **2015**, *15* (6), 4223−4228.

(2) Dou, S.; Xu, H.; Zhao, J.; Zhang, K.; Li, N.; Lin, Y.; Pan, L.; Li, Y. Bioinspired Microstructured Materials for Optical and Thermal Regulation. *Adv. Mater.* **2021**, *33* (6), 2000697.

(3) Kim, K.-C. Effective graded refractive-index anti-reflection coating for high refractive-index polymer ophthalmic lenses. *Mater. Lett.* **2015**, *160*, 158−161.

(4) Born, M.; Wolf, E. *Principles of Optics: Electromagnetic Theory of Propagation, Interference and Diffraction of Light*, 7 ed.; Cambridge University Press: Cambridge, 1999.

(5) Xi, J. Q.; Schubert, M. F.; Kim, J. K.; Schubert, E. F.; Chen, M.; Lin, S.-Y.; Liu, W.; Smart, J. A. Optical thin-film materials with low refractive index for broadband elimination of Fresnel reflection. *Nat. Photonics* **2007**, *1* (3), 176−179.

(6) Pilvi, T.; Puukilainen, E.; Kreissig, U.; Leskelä, M.; Ritala, M. Atomic Layer Deposition of MgF2 Thin Films Using TaF5 as a Novel Fluorine Source. *Chem. Mater.* **2008**, *20* (15), 5023−5028.

(7) Lee, Y.; Sun, H.; Young, M. J.; George, S. M. Atomic Layer Deposition of Metal Fluorides Using HF-Pyridine as the Fluorine Precursor. *Chem. Mater.* **2016**, *28* (7), 2022−2032.

(8) Hennessy, J.; Jewell, A. D.; Greer, F.; Lee, M. C.; Nikzad, S. Atomic layer deposition of magnesium fluoride via bis-

(ethylcyclopentadienyl)magnesium and anhydrous hydrogen fluoride. *Journal of Vacuum Science & Technology A: Vacuum, Surfaces, and Films* **2015**, *33* (1), 01A125−01A125.
(9) Pilvi, T.; Hatanpää, T.; Puukilainen, E.; Arstila, K.; Bischoff, M.; Kaiser, U.; Kaiser, N.; Leskelä, M.; Ritala, M. Study of a novel ALD process for depositing MgF2 thin films. *J. Mater. Chem.* **2007**, *17* (48), 5077−5083.
(10) Wikipedia contributors. (2022, January 10). Magnesium fluoride. In *Wikipedia, The Free Encyclopedia*. Retrieved 23:21, August 19, 2022, from https://en.wikipedia.org/w/index.php?title=Magnesium_fluoride&oldid=1064778163.
(11) Li, N.; Li, Y. D.; Wang, Y. B.; Li, M.; Cheng, Y.; Wu, Y. H.; Zheng, Y. F. Corrosion resistance and cytotoxicity of a MgF2 coating on biomedical Mg-1Ca alloy via vacuum evaporation deposition method. *Surf. Interface Anal.* **2013**, *45* (8), 1217−1222.
(12) Wikipedia contributors. (2022, July 27). Aluminium oxide. In *Wikipedia, The Free Encyclopedia*. Retrieved 23:31, August 19, 2022, from https://en.wikipedia.org/w/index.php?title=Aluminium_oxide&oldid=1100678645.
(13) Berman, D.; Guha, S.; Lee, B.; Elam, J. W.; Darling, S. B.; Shevchenko, E. V. Sequential Infiltration Synthesis for the Design of Low Refractive Index Surface Coatings with Controllable Thickness. *ACS Nano* **2017**, *11* (3), 2521−2530.
(14) Xi, J. Q.; Kim, J. K.; Schubert, E. F. Silica nanorod-array films with very low refractive indices. *Nano Lett.* **2005**, *5* (7), 1385−1387.
(15) Isakov, K.; Kauppinen, C.; Franssila, S.; Lipsanen, H. Superhydrophobic Antireflection Coating on Glass Using Grass-like Alumina and Fluoropolymer. *ACS Appl. Mater. Interfaces* **2020**, *12* (44), 49957−49962.
(16) Han, L.; Zhao, H. Surface antireflection studies of GaN nanostructures with various effective refractive index profiles. *Optics Express* **2014**, *22* (26), 31907−31916.
(17) Kraus, M.; Diao, Z.; Weishaupt, K.; Spatz, J. P.; Täschner, K.; Bartzsch, H.; Schmittgens, R.; Brunner, R. Combined 'moth-eye' structured and graded index-layer anti-reflecting coating for high index glasses. *Opt. Express* **2019**, *27* (24), 34655−34664.
(18) Price, J. J.; Xu, T.; Zhang, B.; Lin, L.; Koch, K. W.; Null, E. L.; Reiman, K. B.; Paulson, C. A.; Kim, C.-G.; Oh, S.-Y.; Oh, J.-K.; Moon, D.-G.; Oh, J.-H.; Mayolet, A.; Williams, C. K.; Hart, S. D. Nanoindentation Hardness and Practical Scratch Resistance in Mechanically Tunable Anti-Reflection Coatings. *Coatings* **2021**, *11* (2), 213.
(19) Koch, K. W.; Lin, L.; Price, J. J.; Kim, C.-G.; Moon, D.-G.; Oh, S.-Y.; Oh, J.-K.; Oh, J.-H.; Paulson, C. A.; Zhang, B.; Subramanian, A.; Mayolet, A.; Williams, C. K.; Hart, S. D. Wavelength-Selective Coatings on Glass with High Hardness and Damage Resistance. *Coatings* **2020**, *10* (12), 1247.
(20) Paulson, C. A.; Price, J. J.; Koch, K. W.; Kim, C.-G.; Oh, J.-H.; Lin, L.; Subramanian, A. N.; Zhang, B.; Amin, J.; Mayolet, A.; Kosik Williams, C.; Hart, S. D. Industrial-grade anti-reflection coatings with extreme scratch resistance. *Opt. Lett.* **2019**, *44* (24), 5977−5977.
(21) Kim, S.; Cho, J.; Char, K. Thermally Stable Antireflective Coatings Based on Nanoporous Organosilicate Thin Films. *Langmuir* **2007**, *108* (9), 8953−8959.
(22) Burghoorn, M.; Roosen-Melsen, D.; De Riet, J.; Sabik, S.; Vroon, Z.; Yakimets, I.; Buskens, P. Single Layer Broadband Anti-Reflective Coatings for Plastic Substrates Produced by Full Wafer and Roll-to-Roll Step-and-Flash Nano-Imprint Lithography. *Materials* **2013**, *6* (9), 3710−3726.
(23) Spinelli, P.; Verschuuren, M. A.; Polman, A. Broadband omnidirectional antireflection coating based on subwavelength surface Mie resonators. *Nat. Commun.* **2012**, *3* (1), 692.
(24) Nostell, P.; Roos, A.; Karlsson, B. Optical and mechanical properties of sol-gel antireflective films for solar energy applications. *Thin Solid Films* **1999**, *351* (1), 170−175.
(25) Price, J. J.; Xu, T.; Zhang, B.; Lin, L.; Koch, K. W.; Null, E. L.; Reiman, K. B.; Paulson, C. A.; Kim, C.-G.; Oh, S.-Y.; Oh, J.-K.; Moon, D.-G.; Oh, J.-H.; Mayolet, A.; Williams, C. K.; Hart, S. D. Nanoindentation Hardness and Practical Scratch Resistance in Mechanically Tunable Anti-Reflection Coatings. *Coatings* **2021**, *11* (2), 213.
(26) Hausner, M. *Specifications and Standards for Optical Coating Durability*; SPIE, 2019.
(27) Du, N.; Robertson, G. P.; Song, J.; Pinnau, I.; Thomas, S.; Guiver, M. D. Polymers of Intrinsic Microporosity Containing Trifluoromethyl and Phenylsulfone Groups as Materials for Membrane Gas Separation. *Macromolecules* **2008**, *41* (24), 9656−9662.
(28) McKeown, N. B. Polymers of Intrinsic Microporosity. *ISRN Mater. Sci.* **2012**, *2012*, 513986.
(29) Ghanem, B. S.; McKeown, N. B.; Budd, P. M.; Fritsch, D. Polymers of Intrinsic Microporosity Derived from Bis(phenazyl)-Monomers. *Macromolecules* **2008**, *41* (5), 1640−1646.
(30) McKeown, N. B.; Budd, P. M.; Msayib, K. J.; Ghanem, B. S.; Kingston, H. J.; Tattershall, C. E.; Makhseed, S.; Reynolds, K. J.; Fritsch, D. Polymers of intrinsic microporosity (PIMs): Bridging the void between microporous and polymeric materials. *Chem. Eur. J.* **2005**, *11* (9), 2610−2620.
(31) Budd, P. M.; Ghanem, B. S.; Makhseed, S.; McKeown, N. B.; Msayib, K. J.; Tattershall, C. E. Polymers of intrinsic microporosity (PIMs): robust, solution-processable, organic nanoporous materials. *Chem. Commun.* **2004**, *4* (2), 230−231.
(32) McGuinness, E. K.; Zhang, F.; Ma, Y.; Lively, R. P.; Losego, M. D. Vapor Phase Infiltration of Metal Oxides into Nanoporous Polymers for Organic Solvent Separation Membranes. *Chem. Mater.* **2019**, *31* (15), 5509−5518.
(33) Ren, Y.; McGuinness, E. K.; Huang, C.; Joseph, V. R.; Lively, R. P.; Losego, M. D. Reaction - Diffusion Transport Model to Predict Precursor Uptake and Spatial Distribution in Vapor-Phase In fi ltration Processes. *Chem. Mater.* **2021**, *33* (13), 5210−5222.
(34) Zhang, F.; McGuinness, E. K.; Ma, Y.; Ren, Y.; Leisen, J. E.; Losego, M. D.; Lively, R. P. Vapor-Phase-Infiltrated AlOx/PIM-1 "Hybrid Scaffolds" as Solution-Processable Amine Supports for CO2 Adsorption. *ACS Applied Polymer Materials* **2021**, *3* (9), 4460−4469.
(35) Berman, D.; Shevchenko, E. Design of functional composite and all-inorganic nanostructured materials via infiltration of polymer templates with inorganic precursors. *Journal of Materials Chemistry C* **2020**, *8* (31), 10604−10627.
(36) Chen, X.; Wu, L.; Yang, H.; Qin, Y.; Ma, X.; Li, N. Tailoring the Microporosity of Polymers of Intrinsic Microporosity for Advanced Gas Separation by Atomic Layer Deposition. *Angew. Chem., Int. Ed.* **2021**, *60* (33), 17875−17880.
(37) Jue, M. L.; McKay, C. S.; McCool, B. A.; Finn, M. G.; Lively, R. P. Effect of Nonsolvent Treatments on the Microstructure of PIM-1. *Macromolecules* **2015**, *48* (16), 5780−5790.
(38) Mason, C. R.; Maynard-Atem, L.; Heard, K. W. J.; Satilmis, B.; Budd, P. M.; Friess, K.; Lanč, M.; Bernardo, P.; Clarizia, G.; Jansen, J. C. Enhancement of CO2 Affinity in a Polymer of Intrinsic Microporosity by Amine Modification. *Macromolecules* **2014**, *47* (3), 1021−1029.
(39) Leng, C. Z.; Losego, M. D. Vapor phase infiltration (VPI) for transforming polymers into organic-inorganic hybrid materials: a critical review of current progress and future challenges. *Materials Horizons* **2017**, *4* (5), 747−771.
(40) Waldman, R. Z.; Mandia, D. J.; Yanguas-Gil, A.; Martinson, A. B. F.; Elam, J. W.; Darling, S. B. The chemical physics of sequential infiltration synthesis—A thermodynamic and kinetic perspective. *J. Chem. Phys.* **2019**, *151* (19), 190901.
(41) Biswas, M.; Libera, J. A.; Darling, S. B.; Elam, J. W. New insight into the mechanism of sequential infiltration synthesis from infrared spectroscopy. *Chem. Mater.* **2014**, *26* (21), 6135−6141.
(42) Chen, Z.; He, C.; Li, F.; Tong, L.; Liao, X.; Wang, Y. Responsive Micellar Films of Amphiphilic Block Copolymer Micelles: Control on Micelle Opening and Closing. *Langmuir* **2010**, *26* (11), 8869−8874.
(43) Yang, G. G.; Choi, H. J.; Han, K. H.; Kim, J. H.; Lee, C. W.; Jung, E. I.; Jin, H. M.; Kim, S. O. Block Copolymer Nanopatterning

https://doi.org/10.1021/acsnano.2c05592
ACS Nano 2022, 16, 14754−14764

for Nonsemiconductor Device Applications. *ACS Appl. Mater. Interfaces* **2022**, *14* (10), 12011−12037.
(44) Peng, Q.; Tseng, Y. C.; Darling, S. B.; Elam, J. W. A route to nanoscopic materials via sequential infiltration synthesis on block copolymer templates. *ACS Nano* **2011**, *5* (6), 4600−4606.
(45) Wang, Y. Nondestructive Creation of Ordered Nanopores by Selective Swelling of Block Copolymers: Toward Homoporous Membranes. *Acc. Chem. Res.* **2016**, *49* (7), 1401−1408.
(46) Yin, J.; Yao, X.; Liou, J. Y.; Sun, W.; Sun, Y. S.; Wang, Y. Membranes with highly ordered straight nanopores by selective swelling of fast perpendicularly aligned block copolymers. *ACS Nano* **2013**, *7* (11), 9961−9974.
(47) Berman, D.; Shevchenko, E. Design of functional composite and all-inorganic nanostructured materials via infiltration of polymer templates with inorganic precursors. *J. Mater. Chem. C* **2020**, *8* (31), 10604.
(48) Waldman, R. Z.; Mandia, D. J.; Yanguas-Gil, A.; Martinson, A. B. F.; Elam, J. W.; Darling, S. B. The chemical physics of sequential infiltration synthesis—A thermodynamic and kinetic perspective. *J. Chem. Phys.* **2019**, *151* (19), 190901.
(49) Losego, M. D.; Peng, Q. Atomic Layer Deposition and Vapor Phase Infiltration. *Surface Modification of Polymers* **2019**, 135−159.
(50) Han, H.; Jeong, B.; Park, T. H.; Cha, W.; Cho, S. M.; Kim, Y.; Kim, H. H.; Kim, D.; Ryu, D. Y.; Choi, W. K.; Park, C. Highly Photoluminescent and Environmentally Stable Perovskite Nanocrystals Templated in Thin Self-Assembled Block Copolymer Films. *Adv. Funct. Mater.* **2019**, *29* (26), 1808193.
(51) Matsushita, Y.; Mori, K.; Saguchi, R.; Nakao, Y.; Noda, I.; Nagasawa, M. Molecular weight dependence of lamellar domain spacing of diblock copolymers in bulk. *Macromolecules* **1990**, *23* (19), 4313−4316.
(52) Onbaşlı, M. C.; Tandia, A.; Mauro, J. C. *Mechanical and Compositional Design of High-Strength Corning Gorilla® Glass BT - Handbook of Materials Modeling: Applications: Current and Emerging Materials*; Andreoni, W., Yip, S., Eds.; Springer International Publishing: Cham, 2018; pp 1−23.
(53) Price, J. J.; Xu, T.; Zhang, B.; Lin, L.; Koch, K. W.; Null, E. L.; Reiman, K. B.; Paulson, C. A.; Kim, C.-g.; Oh, S.-y.; Oh, J.-k.; Moon, D.-g.; Oh, J.-h.; Mayolet, A.; Williams, C. K.; Hart, S. D. Nanoindentation Hardness and Practical Scratch Resistance in Mechanically Tunable Anti-Reflection Coatings. *Coatings* **2021**, *11* (2), 213.
(54) Zheng, L.; Schmid, A. W.; Lambropoulos, J. C. Surface effects on Young's modulus and hardness of fused silica by nanoindentation study. *J. Mater. Sci.* **2007**, *42* (1), 191−198.
(55) Chen, X.; Xiang, Y.; Vlassak, J. J. Novel technique for measuring the mechanical properties of porous materials by nanoindentation. *J. Mater. Res.* **2006**, *21* (3), 715−724.
(56) Tayebi, N.; Polycarpou, A. A.; Conry, T. F. Effects of substrate on determination of hardness of thin films by nanoscratch and nanoindentation techniques. *J. Mater. Res.* **2004**, *19* (6), 1791−1802.
(57) Bakhti, H.; Laghrissi, A.; Roth, A.; Azrar, L.; Es-Souni, M. Nanomechanical characterization and modeling of anodized porous aluminum oxide thin films with photografted anti - biofouling polymer brushes on their pore walls. *Appl. Nanosci.* **2020**, *10* (7), 2139−2151.
(58) Ryu, K.; Lee, Y. J.; Ju, M.; Choi, H.; Kim, B.; Lee, J.; Oh, W.; Choi, K.; Balaji, N.; Yi, J. Optimal indium tin oxide layer as anti reflection coating for crystalline silicon solar cell with shallow emitter. *Thin Solid Films* **2012**, *521*, 50−53.
(59) Sung, Y.; Malay, R. E.; Wen, X.; Bezama, C. N.; Soman, V. V.; Huang, M.-H.; Garner, S. M.; Poliks, M. D.; Klotzkin, D. Anti-reflective coating with a conductive indium tin oxide layer on flexible glass substrates. *Appl. Opt.* **2018**, *57* (9), 2202−2202.
(60) Al Kutubi, H.; Rassaei, L.; Olthuis, W.; Nelson, G. W.; Foord, J. S.; Holdway, P.; Carta, M.; Malpass-Evans, R.; McKeown, N. B.; Tsang, S. C.; Castaing, R.; Forder, T. R.; Jones, M. D.; He, D.; Marken, F. Polymers of intrinsic microporosity as high temperature templates for the formation of nanofibrous oxides. *RSC Adv.* **2015**, *5* (89), 73323−73326.
(61) She, Y.; Goodman, E. D.; Lee, J.; Diroll, B. T.; Cargnello, M.; Shevchenko, E. V.; Berman, D. Block-Co-polymer-Assisted Synthesis of All Inorganic Highly Porous Heterostructures with Highly Accessible Thermally Stable Functional Centers. *ACS Appl. Mater. Interfaces* **2019**, *11* (33), 30154−30162.
(62) Berman, D.; Sha, Y.; Shevchenko, E. V. Effect of Polymer Removal on the Morphology and Phase of the Nanoparticles in All-Inorganic Heterostructures Synthesized via Two-Step Polymer Infiltration. *Molecules* **2021**, *26* (3), 679.
(63) Pleshek, D.; Tran, J.; Li, Y.; Shirani, A.; Shevchenko, E. V.; Berman, D. Swelling-Assisted Sequential Infiltration Synthesis of Nanoporous ZnO Films with Highly Accessible Pores and Their Sensing Potential for Ethanol. *ACS Appl. Mater. Interfaces* **2021**, *13* (30), 35941−35948.

https://doi.org/10.1021/acsnano.2c05592
ACS Nano 2022, 16, 14754−14764